Climatology of Sign Reversals of the Meridional Potential Vorticity Gradient over Africa and Australia

MICHAEL DICKINSON AND JOHN MOLINARI

Department of Earth and Atmospheric Sciences, University at Albany, State University of New York, Albany, New York

(Manuscript received 9 August 1999, in final form 18 April 2000)

ABSTRACT

A 10-yr climatology (1986–95) was performed using ECMWF gridded analyses on isentropic surfaces to identify regions where the lower-tropospheric meridional potential vorticity (PV) gradient changes sign across Africa and Australia during their respective summer seasons. While an African sign reversal has been documented, no similar study has been performed for the Australian region, which also has desert on the poleward side of open ocean. In each hemisphere, a northward decrease of PV is sufficient to produce a sign reversal.

It was found that PV decreases northward in the lower troposphere across northern Australia, with the maximum reversal on the 315-K surface. It had comparable magnitude but smaller zonal extent (~3000 km) than that on the 320-K surface in Africa (~5000 km). In each region the sign reversal was associated with cyclonic PV anomalies on the equatorward side and anticyclonic anomalies on the poleward side.

OLR was used as a proxy for deep convective heating in order to evaluate the total convective forcing of PV. The vertical distribution of heating was specified. In both regions the maximum total convective forcing of PV was largest on the equatorward edge of the sign reversal region. The effects of dry convection were not included in the PV budget. Dry convection, located poleward of the maximum deep convection, acts as a lower-tropospheric PV sink and produces anticyclonic PV anomalies. In both regions these anticyclonic anomalies were larger in magnitude and areal coverage than the cyclonic anomalies associated with deep convection.

The potential instability implied by the sign reversal regions has traditionally been associated with the growth of easterly waves. In support of this argument, bandpass-filtered (2–6 day) meridional wind variance on the 320-K surface nearly triples from east to west along the African sign reversal. In Australia, little evidence was found of such waves in the 2–10-day meridional wind variance. Possible explanations for the lack of growing disturbances over Australia are discussed.

1. Introduction

Since the work of Riehl (1954), easterly waves have received considerable attention in the literature, much of which focused on waves generated over Africa (Carlson 1969; Burpee 1972; Reed et al. 1977; Albignat and Reed 1980; Thorncroft and Hoskins 1994a,b; Pytharoulis and Thorncroft 1999). African easterly waves (AEWs) are typically found during the Northern Hemisphere summer between 10° and 20°N. They originate in eastern Africa (Burpee 1972; Albignat and Reed 1980) and reach a maximum amplitude near the West African coast. AEWs have a period of 2–6 days, a wavelength of 2000–4000 km, and a phase speed of approximately 8 m s^{-1} (Burpee 1972; Reed et al. 1977). It is believed that over half of the tropical cyclones in the Atlantic basin form in association with AEWs (Frank 1970; Avila and Clark 1989). AEWs may also be important in triggering tropical cyclogenesis in the eastern Pacific (Simpson et al. 1969; Avila and Pasch 1992).

The source of AEWs was proposed by Burpee (1972), who showed that AEW generation was directly linked to the presence of a 700-hPa easterly jet. This African easterly jet (AEJ) is associated with a strong positive meridional temperature gradient in the lower troposphere and a reversal of the temperature gradient in the middle troposphere (Burpee 1972). Recently Cook (1999) noted the importance of the poleward decrease of surface moisture in the production and maintenance of the AEJ. Using a simple GCM with specified surface temperature gradients, Thorncroft and Blackburn (1999) argued that the AEJ is forced by two separate diabatic heating sources: the deep cumulus convection to the south in the ITCZ and the dry convection over the Sahara desert. Brikas and Thorncroft (1999) recently supported this result using European Centre for Medium-Range Forecasts (ECMWF) reanalysis data.

Burpee (1972) found that the meridional gradient of Ertel potential vorticity (PV) changed sign near 700 hPa

Corresponding author address: Michael Dickinson, Department of Earth and Atmospheric Sciences, University at Albany, State University of New York, Albany, NY 12222.
E-mail: mjd@atmos.albany.edu

over Africa. This sign reversal of the meridional PV gradient (q_y) satisfies a necessary condition for instability of the mean flow (Charney and Stern 1962). AEWs grow through an instability arising from the horizontal and vertical shears of the mean flow. Observational results by Norquist et al. (1977) and recent idealized modeling simulations by Thorncroft and Hoskins (1994a,b) have shown both barotropic and baroclinic processes contribute to African wave growth. Calculated growth rates by Lau and Lau (1990) also show wave growth along the sign reversal region of Africa.

Schubert et al. (1991) found that an idealized ITCZ convective heating produced a positive PV anomaly below the convective heating, resulting in a change of sign of the lower-tropospheric meridional PV gradient on the poleward side of the heating. Both Thorncroft and Blackburn (1999) and Brikas and Thorncroft (1999) show that, in addition to the positive PV anomaly associated with the ITCZ convection, a negative anomaly is present north of the AEJ associated with the dry convection over the Saharan desert. Thorncroft and Blackburn (1999) found that the dry convective heating was especially important in preserving the AEJ and its associated meridional gradients of PV.

While a number of studies have focused on Africa, much less research has been done concerning disturbances in the easterlies in the Southern Hemisphere. The alignment of the geography in Australia is similar to that found in West Africa. Both regions have ocean on the equatorward side of a large inland desert. Since the AEJ and sign reversal of the meridional PV gradient are related to the distribution of ocean and desert over Africa, it seems likely that, given a similar distribution in the Australian region, an easterly jet and a sign reversal would also be present there. Schubert et al. (1991) suggested that the relationship between ITCZ heating and the change of sign of the meridional PV gradient is not unique to West Africa and that a similar evolution may occur in the tropical east Pacific and northern Australia. However, no sign reversal of the meridional PV gradient has been documented in the Australian region.

According to McBride and Keenan (1982), easterly waves that fit the AEW criteria presented by Burpee (1972) and Reed et al. (1977) are extremely rare in the Australian region. Using twice-daily satellite images, they found only one AEW-type disturbance in the easterlies during the period of their study (1974–79). Carlson (1969) and Avila and Pasch (1992) note, however, that easterly waves are often difficult to track using satellite images. Nakazawa (1986) showed power in 3–10-day filtered outgoing longwave radiation (OLR) along the northwestern and northeastern coasts of Australia during the Southern Hemisphere summer, suggesting the importance of synoptic-scale disturbances in the region.

No long-term sign reversal climatology has been performed for either Africa or Australia. In addition, easterly wave studies have been performed using only one or two summers of observations (Burpee 1972, 1974; Albignat and Reed 1980; Nitta et al. 1985; Nakazawa 1986) or model analyses (Nitta et al. 1985). The purpose of this study is to compute a summer season climatology of the sign reversal of the meridional PV gradient for the African and Australian regions, and to determine the role of convective forcing in its generation. In addition, the analyses are examined for evidence of synoptic-scale disturbances to determine if sign reversals of the meridional PV gradient are correlated with disturbance growth.

2. Data and methodology

This study employed 10 years (1986–95) of twice-daily ECMWF uninitialized gridded analyses obtained from the National Center for Atmospheric Research. The data were obtained on a 1.125° latitude–longitude grid on 12 pressure levels. Ertel PV was calculated on isentropic surfaces following Molinari et al. (1995) using

$$q = g\sigma^{-1}(\zeta_\theta + f), \tag{1}$$

where $\sigma = -\partial p/\partial\theta$.

Previous studies support the use of ECMWF analyses in the Tropics. ECMWF gridded analyses have been used to study synoptic- and planetary-scale tropical waves (e.g., Reed et al. 1988; Liebmann and Hendon 1990; Lau and Lau 1990; Dunkerton and Baldwin 1995; Harrison and Vecchi 1997; Molinari et al. 1997, 2000). Although the studies focused on waves of different spatial and temporal scales, each showed that there was excellent agreement between the ECMWF gridded analyses and independently derived observational data, such as OLR. Furthermore, Molinari et al. (1997), Tomas and Webster (1997), and Tomas et al. (1999) have shown that time-averaged features, such as the ITCZ, are well represented in the ECMWF analyses.

OLR will be used as a proxy for deep tropical convection. A 10-yr, twice-daily OLR dataset was obtained from the Cooperative Institute for Research in Environmental Sciences on a 2.5° latitude–longitude global grid. This dataset was described by Liebmann and Smith (1996).

It is well documented that African easterly waves have their maximum power within the 2–6-day range (Burpee 1972; Reed et al. 1977; Albignat and Reed 1980). Both the meridional component of the horizontal wind (v) and the OLR in this study are bandpass filtered (Lanczos 1956; Duchon 1979) with cutoff periods of 2 and 6 days, denoted by $\tilde{V}_{2-6}$ and $\widetilde{\mathrm{OLR}}_{2-6}$, to attempt to isolate the wave-scale disturbances from the diurnal and low-frequency variations.

In the Pacific basin, Nitta et al. (1985) and Lau and Lau (1990) found that peaks in the power spectra during the Northern Hemisphere summer range from 4 to 5 days in the central North Pacific to 6 to 8 days in the western North Pacific. Chang et al. (1996) found a peak

in the power spectra in the 8–9-day range in the western North Pacific. Since the preferred timescale of disturbances is unknown in the Southern Hemisphere, both 2–6- and 2–10-day periods (denoted by $\tilde{V}_{2-10}$ and $\widetilde{\mathrm{OLR}}_{2-10}$) are examined in this study. Disturbances with the same periods as easterly waves, such as tropical cyclones or midlatitude synoptic systems extending into the subtropics, will also be captured by the bandpass-filtering process.

Of interest in this paper is the generation of PV by diabatic heating associated with cumulus convection and its influence on the sign reversal of the meridional PV gradient on an isentropic surface. In the presence of convection, parcels will not remain on isentropic surfaces. To account for this, the term $\dot{\theta}\partial q/\partial\theta$ within dq/dt is moved to the rhs of the PV equation and treated as an additional source term. The PV equation is then given by

$$\left.\frac{dq}{dt}\right|_{\theta} = -\dot{\theta}\frac{\partial q}{\partial\theta} + g\sigma^{-1}[(\boldsymbol{\nabla}\times\mathbf{V} + f\hat{\mathbf{k}})\cdot\boldsymbol{\nabla}\dot{\theta}] + g\sigma^{-1}\hat{\mathbf{k}}\cdot(\boldsymbol{\nabla}_{\theta}\times\mathbf{F}), \quad (2)$$

where $dq/dt|_{\theta}$ denotes a time derivative following the flow on an isentropic surface, $\mathbf{V} = u\hat{\mathbf{i}} + v\hat{\mathbf{j}}$, $\boldsymbol{\nabla}_{\theta} = \hat{\mathbf{i}}\partial/\partial x|_{\theta} + \hat{\mathbf{j}}\partial/\partial y|_{\theta}$, and $\boldsymbol{\nabla} = \boldsymbol{\nabla}_{\theta} + \hat{\mathbf{k}}\partial/\partial\theta$. The first rhs term in Eq. (2) will be referred to as the vertical advection of PV, which is often small enough to neglect (Rodwell and Hoskins 1995). The second rhs term will be referred to as the convective generation of PV and is valid following a parcel in three dimensions. The sum of the first two rhs terms represents the total convective forcing of PV following the flow on an isentropic surface. The third rhs term of Eq. (2) represents the effect of friction. Since the level of interest is above the friction layer, this term will not be computed.

OLR is bilinearly interpolated to the same grid resolution as the ECMWF analyses. Vertically integrated convective heating (in °C day^{-1}) is estimated from OLR by

$$\frac{1}{\theta_t - \theta_o}\int_{\theta_o}^{\theta_t}\dot{\theta}\,d\theta = \begin{cases}\dfrac{255 - \mathrm{OLR}}{15} & \mathrm{OLR} < 255\ \mathrm{W\ m^{-2}}\\ 0 & \mathrm{OLR} \geq 255\ \mathrm{W\ m^{-2}}\end{cases} \quad (3)$$

(G. Kiladis and B. Liebmann 1998, personal communication), where θ_o and θ_t are 300 and 360 K, respectively. This form is based in part on the correlation between (255−OLR) and upper-tropospheric divergence in the Tropics found by Sardeshmukh and Liebmann (1993). Equation (3) gives a range of convective heating of approximately 0–12°C day^{-1}. To validate the convective heating values obtained from Eq. (3), time-averaged diabatic heating was calculated from three precipitation datasets: the Geostationary Operational Environmental Satellite (GOES) Precipitation Index (Arkin and Meisner 1987; Janowiak and Arkin 1991), Global Precipitation Climatology Project version 1c satellite–gauge precipitation product (Huffman et al. 1995), and Climate Prediction Center (CPC) Merged Analysis of Precipitation (Xie and Arkin 1997). Each dataset produced values of vertically integrated convective heating over the Tropics quite similar to Eq. (3) (not shown). Equation (3) is designed to represent only the influence of deep convection, which acts to modify the PV field by producing positive PV anomalies below the level of maximum heating (Raymond 1992). The effects of radiative cooling and sensible heat flux from the ground are not included by this relation. Thus Eq. (3) does not measure the influence of dry convection.

The first two rhs terms of Eq. (2) were calculated using the twice-daily ECMWF and OLR data at tropospheric isentropic levels 310, 315, and 320 K. A vertical structure for the heating must be specified in order to calculate $\partial\dot{\theta}/\partial\theta$ in Eq. (2). A simple linear vertical profile in $\dot{\theta}$ is assumed, from zero at 300 K to a maximum at 330 K, and linearly back to zero at 360 K. The maximum at 330 K is taken as twice the vertically integrated value in order to be consistent with Eq. (3). A similar vertical distribution of convective heating over Africa was assumed by Thorncroft and Blackburn (1999). Because the PV budget in this paper is computed only below 330 K (the assumed level of maximum heating), the vertical component of the second right-hand side term in Eq. (2) always acts to increase PV as long as absolute vorticity is positive.

Some support exists for the assumed simple linear vertical profile of heating in the lower troposphere. Houze (1997, his Fig. 8) showed that the sum of convective and associated stratiform heating in the Tropics produces convergence from 950 to 400 mb. To a good approximation (assuming adiabatic cooling balances the heating and stability varies slowly in the vertical in the lower troposphere) this implies an upward increase in heating and PV generation in the same layer. This layer encompasses the 310–320-K isentropic levels considered in this study. In addition, Rodwell and Hoskins (1995) calculated a vertical heating profile from ECMWF gridded analyses as a residual from the time-averaged thermodynamic budget. In a region of strong tropical convection, the time-averaged vertical profile of heating (their Fig. 3) increased upward nearly linearly in a layer from sigma levels 0.95 to 0.35. Thus the assumed linear profile of diabatic heating is consistent with the profile occurring in the model that produces the gridded analyses of other variables. The benefit of using ''observed'' heating from OLR rather than model-derived heating is that it gives some confidence that the spatial distribution of heating is accurate and omits potential cumulus parameterization problems in the model. It will be shown that the generation of PV by deep convection using Eq. (2) and Eq. (3) is consistent in both location and magnitude with the analyzed positive lower-tropospheric PV anomalies, thus giving confi-

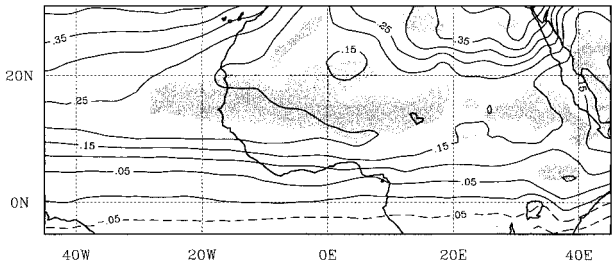

FIG. 1. The 10-yr summertime (1 Jul–31 Oct) mean PV (in PVU, 1 PVU = 10^{-6} K m^2 kg^{-1} s^{-1}; contoured) and region of meridional PV gradient less than zero (shaded) on the 320-K surface. Contour interval for PV is 0.05 PVU.

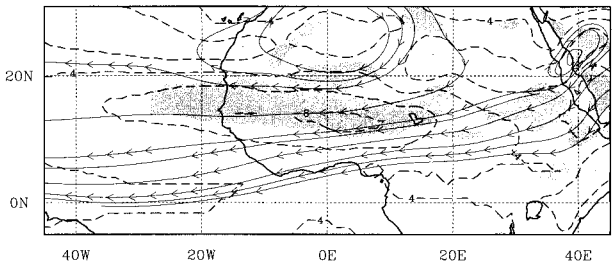

FIG. 2. As in Fig. 1 but for isotachs (contoured) and streamlines. Contour interval for isotachs is 2 m s^{-1}.

dence in both the analyses and the simple assumptions of the heating profile.

The intent of the PV budget analysis in this study is to identify the pattern of convective forcing associated with the maintenance of the sign reversal regions in Africa and Australia. The role of the easterly waves (eddies) in the destruction of the sign reversal regions through horizontal mixing of PV will not be considered here.

Although AEWs are generated from May to November (Avila and Pasch 1992), the strongest waves are generally found from July to October. The period 1 July–31 October was chosen to calculate time means for the African region. Since no easterly wave climatology exists for the Australian region, the averaging period was chosen to encompass the most active period for tropical depressions in the area. Based on the results of McBride (1995, his Figs. 3.9e,f) the period 1 December–31 March was chosen for the Australian basin. All results, including the PV budget, will be displayed as 10-yr means of the 4-month period.

3. Results

a. Africa

The July–October 10-yr mean fields for Africa are now shown. Since the amplitude of the AEJ is largest near 650 hPa and the amplitude of AEWs is largest near 700 hPa (Burpee 1972; Reed et al. 1977), the 320-K surface, which is near the 650-hPa surface across interior Africa, is used. The mean PV and the region where the mean meridional PV gradient ($\overline{q_y}$, calculated as the average of q_y) is less than zero (shaded) on the 320-K surface are shown in Fig. 1. The value of the time-averaged PV increases rapidly from the equator to about 12°N, where the PV reaches a maximum. Poleward of 12°N the mean PV decreases slowly, reaching a minimum just poleward of 20°N across the Saharan desert. The sign reversal also exists on lower isentropic surfaces (310 and 315 K) but is most intense and covers the largest area on the 320-K surface. The Charney–Stern criterion is satisfied between 12° and 20°N from nearly 30°W to 20°E.

An additional necessary condition for instability of the mean flow, the Fjortoft condition (Fjortoft 1950; also see Eliassen 1983), requires that the mean zonal current be positively correlated with $\overline{q_y}$. Figure 2 shows that the mean AEJ is collocated with the sign reversal across Africa in the summertime mean fields, which satisfies the Fjortoft necessary condition for instability.

The PV anomalies were calculated by $\overline{q} - gf/[\overline{\sigma}]$, where the overbar represents a time mean and the brackets represent an average over the plotting domain shown for Africa (Fig. 1) or for Australia (Fig. 8). The term $gf/[\overline{\sigma}]$ represents the background PV that would exist if there were no motion and constant static stability. Under those circumstances only f would contribute to the spatial variation of PV. This background value is analogous to the ''standard potential vorticity'' given by Eq. (15) of Hoskins et al. (1985), but with time- and area-averaged stability from a given region replacing the standard atmosphere stability. The PV anomaly in this paper is defined as the difference between the time-averaged total PV and this background value. The results (Fig. 3) show a cyclonic[1] PV anomaly equatorward of 15°N extending from the eastern Atlantic across Africa. The strongest cyclonic PV anomalies are found west of 10°E. Anticyclonic PV anomalies are found poleward of 15°N across northern Africa and extending into the eastern Atlantic. The strongest anticyclonic anomalies are found poleward of 20°N across the Sahara Desert.

Thorncroft and Blackburn (1999) and Brikas and Thorncroft (1999) have argued that the AEJ is a result of deep cumulus convection to the south and dry convection over the Sahara. Strong surface heating over the Saharan Desert leads to an upward decrease in diabatic heating in the lower troposphere, which, according to second rhs term in Eq. (2), produces an anticyclonic PV anomaly. Furthermore, the presence of a deep mixed layer ($\partial\theta/\partial p \approx 0$) over the Sahara maintains near-zero PV in the lower troposphere. The anticyclonic PV anomaly, which shows clearly in Fig. 3, is a result of dry

[1] To avoid confusing terminology, PV anomalies that are of the same sign as the Coriolis parameter in each hemisphere will be called cyclonic, and those of opposite sign will be called anticyclonic.

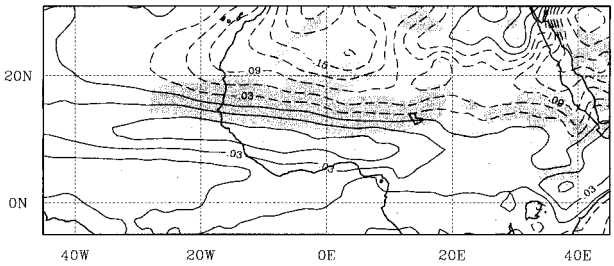

FIG. 3. As in Fig. 1 but for PV anomalies, given by $\overline{q} - gf/[\overline{\sigma}]$ (contoured). Contour interval is 0.03 PVU.

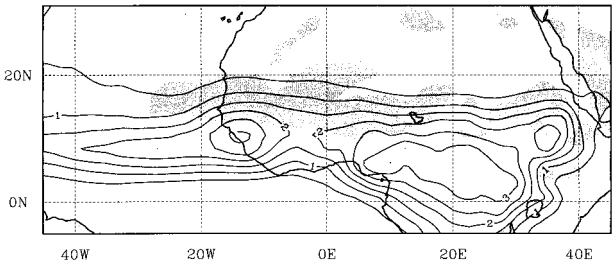

FIG. 4. As in Fig. 1 but for vertically integrated diabatic heating from Eq. (3) (contoured). Contour interval is 0.5°C day^{-1}.

convection and cannot be represented by the assumed OLR–diabatic heating relationship given by Eq. (3). The anticyclonic PV anomaly, in combination with the cyclonic PV anomaly generated by the moist convection to the south, produce the change in sign of $\overline{q_y}$.

The magnitude of the negative PV anomaly over the Sahara is substantially greater than that of the positive PV anomaly to the south. This suggests that dry convection plays more of a role in generating the $\overline{q_y}$ sign reversal than does moist convection farther south. Thorncroft and Blackburn (1999) came to the same conclusions on the basis of their numerical simulations of the AEJ.

The relationship between the sign reversal and the vertically integrated diabatic heating [from Eq. (3)] is presented in Fig. 4. The location of the sign reversal appears to be related closely to the distribution of deep convective heating. Across Africa the sign reversal is present where the mean meridional gradient of convective heating is largest and negative, with the strongest cumulus convection just on the equatorward side.

The convective generation of PV [the second term on the rhs of Eq. (2)], time-averaged over 10 summers, is shown in Fig. 5a. The PV generation is largest on the equatorward edge of the sign reversal on the cyclonic shear side of the easterly jet (Fig. 2) but just poleward of the maximum convective heating (Fig. 4). This term is not maximized in the region of largest convective heating but where the product of q (Fig. 1) and the vertical gradient of diabatic heating is largest. Given the assumed linear vertical heating profile, the latter is largest when the OLR is lowest.

The effect of the vertical advection of PV [first term of the rhs of Eq. (2)] is shown in Fig. 5b. A comparison of Fig. 5b with Fig. 5a shows that although the vertical advection term is, on average, nearly 3 times smaller than convective PV generation, the vertical advection term cannot be ignored. Because $\dot{\theta}$ in Eq. (3) is always positive, the sign of the vertical advection depends on the vertical distribution of PV. Across Africa the vertical advection term is negative, indicating that lower values of PV are being advected upward to the 320-K surface. From central to west Africa, the largest advection is found within the sign reversal, on the poleward side of the convective PV generation maximum (Fig. 5a).

The total convective forcing of PV on an isentropic surface [the sum of the first two terms on the rhs of Eq. (2)] is presented in Fig. 5c. The vertical advection term (Fig. 5b) acts to oppose the convective generation term (Fig. 5a), especially within the sign reversal region. As a result, the sum of the two terms produces a strong negative meridional gradient of total convective forcing on the equatorward edge of the sign reversal region. This gradient is responsible for the location of the sign reversal.

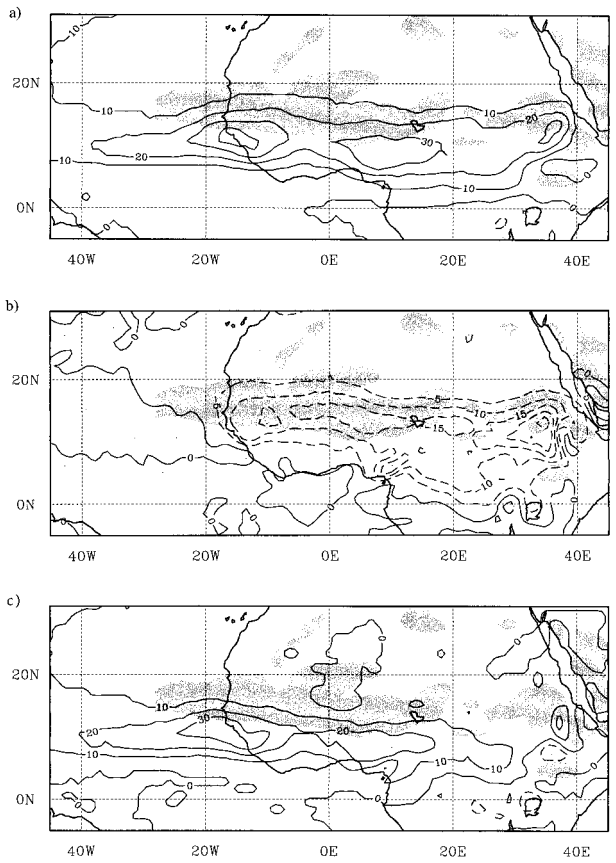

FIG. 5. As in Fig. 1 but for (a) convective generation of PV [second rhs term in Eq. (2)], (b) vertical advection of PV [first rhs term in Eq. (2)], and (c) total convective forcing of PV [sum of (a) and (b)]. Contour interval is (a) 10×10^{-3}, (b) 5×10^{-3}, and (c) 10×10^{-3} PVU day^{-1}.

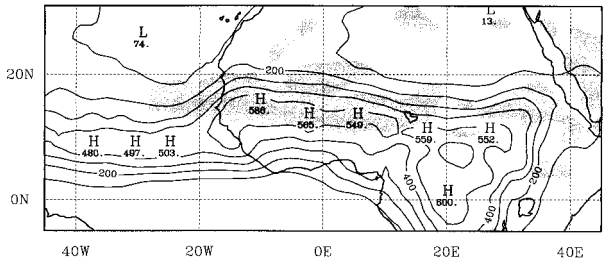

FIG. 6. As in Fig. 1 but for 2–6-day OLR variance (contoured). Contour interval is 100 W^2 m^{-4}.

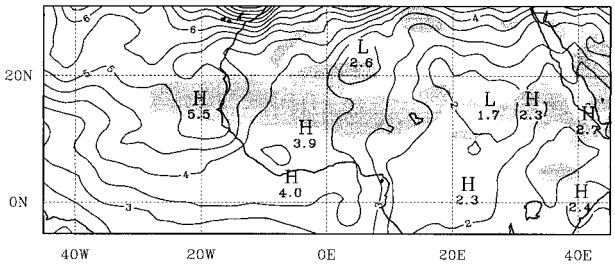

FIG. 7. As in Fig. 1 but for 2–6-day v variance (contoured). Contour interval is 0.5 m^2 s^{-2}.

Mean flow streamlines (Fig. 2) show that the flow is generally easterly across Africa to the Atlantic Ocean. Parcels would continually gain PV as they move from east to west in the generation region (Fig. 5c). The location of the maximum total convective forcing of PV (Fig. 5c) is in excellent agreement with the location of the cyclonic PV anomaly (Fig. 3) over Africa. The mean flow in Fig. 2 suggests that on average a parcel will move at 5 m s^{-1} and travel about 2500 km before leaving the region of large convective forcing of PV (Fig. 5c). Over the 6 days of its passage, assuming an average PV forcing of 20×10^{-3} PVU day^{-1}, PV would change on the order of 0.1 PVU, which is consistent with the order of magnitude of the PV anomaly field shown in Fig. 3. The results from Eq. (2) arise from using two independent datasets, observed OLR data, and ECMWF analyses. The consistent relationship between the gridded analysis-derived PV gradient and the OLR-derived total convective forcing PV give confidence in the ECMWF analyses.

Burpee (1972) suggested that AEWs grow through an instability arising from the horizontal and vertical shears of the mean flow. Recent modeling studies by Thorncroft and Hoskins (1994a,b) have shown easterly wave growth when a sign reversal of q_y is present. To address disturbance growth in the vicinity of the sign reversal using observations and model analyses, Figs. 6 and 7 show the mean $\widetilde{\mathrm{OLR}}_{2-6}$ variance ($\widetilde{\mathrm{OLR}}_{2-6}$ squared) and mean $\tilde{V}_{2-6}$ variance for the 10-yr period.

The axis of maximum OLR_{2-6} variance (Fig. 6) is oriented along the equatorward edge of the sign reversal and is on the poleward side of the maximum deep convection (Fig. 4). The $\widetilde{\mathrm{OLR}}_{2-6}$ variance accounts for 25%–35% of the total unfiltered OLR variance across Africa. The position of the $\widetilde{\mathrm{OLR}}_{2-6}$ variance maximum corresponds to the area of large low-level θ_e (see Fig. 2b of Thorncroft and Haile 1995 and Fig. 4a of Hodges and Thorncroft 1997) and to the location of mesoscale convective complexes (Laing and Fritsch 1997) and other convective activity, such as squall lines (Thorncroft and Haile 1995; Hodges and Thorncroft 1997) and easterly waves (Burpee 1972; Reed et al. 1977). The $\widetilde{\mathrm{OLR}}_{2-6}$ variance is weak in extreme eastern Africa, but grows rapidly westward between 35° and 30°E (west of the East African highlands). The variance grows slowly (less than 10% increase along the sign reversal) west of 30°E over Africa. The small increase of $\widetilde{\mathrm{OLR}}_{2-6}$ variance across central and western Africa (compared to the large increase between 30° and 40°E) suggests that significant easterly wave growth is not indicated by the filtered OLR. One possible explanation is that easterly waves are masked by other convective phenomena, such as squall lines, which are able to propagate through the wave. Off the African coast, the $\widetilde{\mathrm{OLR}}_{2-6}$ variance maximum is located nearer to the equator and is weaker, a response to the cold Canary Current in the eastern Atlantic. Carlson (1969) found that waves were unable to maintain convection and weakened over the cooler waters off Africa. The location of large $\widetilde{\mathrm{OLR}}_{2-6}$ variance across Africa is quite similar to the results of Nitta et al. (1985) and Nakazawa (1986).

The $\tilde{V}_{2-6}$ variance (Fig. 7) is small across eastern Africa. From 25°E to 20°W variance values approximately triple in magnitude along the sign reversal region. In western Africa the $\tilde{V}_{2-6}$ variance accounts for roughly 50% of the total unfiltered v variance. Most rapid variance growth is found in extreme western Africa and the eastern Atlantic, between 10° and 20°W. The location of the maximum variance is similar to that shown by Albignat and Reed (1980) and Nitta et al. (1985). West of the $\tilde{V}_{2-6}$ variance maximum at 20°W, the axis of maximum $\tilde{V}_{2-6}$ variance extends southeastward and is collocated with the $\widetilde{\mathrm{OLR}}_{2-6}$ variance maximum (Fig. 6) within the ITCZ. In this region the $\tilde{V}_{2-6}$ variance accounts for over 60% of the total unfiltered v variance.

Calculation of the mean eddy kinetic energy (EKE) for the 10-yr period (not shown) shows a similar pattern to the $\tilde{V}_{2-6}$ variance. Pytharoulis and Thorncroft (1999) calculated the seasonal mean EKE for the 1995 summer over Africa. Though the magnitude was larger, the pattern was similar to the 10-yr mean EKE. The interannual shift of the African jet may explain the lower magnitudes of EKE in the 10-yr mean compared to 1995.

The implied increase in disturbance amplitude across Africa, as measured by $\tilde{V}_{2-6}$ variance, is supported by the observational results of Pytharoulis and Thorncroft (1999), the modeling simulations of Thorncroft and Hoskins (1994a,b), and by the growth rate calculation of Lau and Lau (1990). In addition, Lau and Lau (1990) show large decay rates over the eastern and central At-

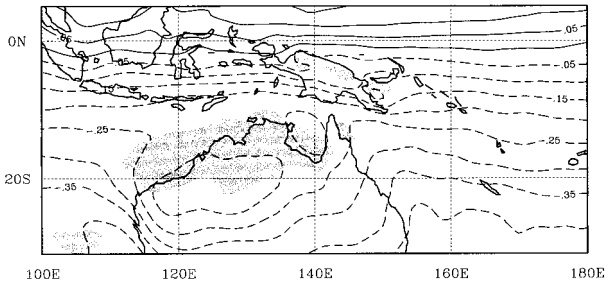

FIG. 8. The 10-yr summertime (1 Dec–31 Mar) mean PV (contoured) and region of meridional PV gradient less than zero (shaded) on the 315-K surface. Contour interval for PV is 0.05 PVU.

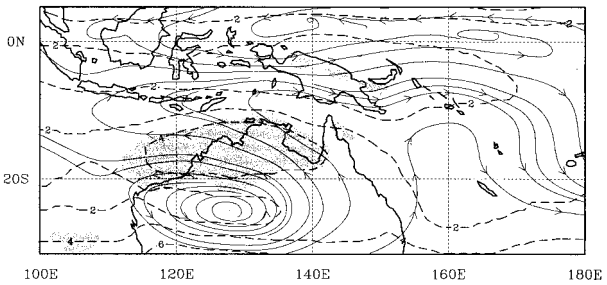

FIG. 9. As in Fig. 8 but for isotachs (contoured) and streamlines. Contour interval for isotachs is 2 m s^{-1}.

lantic in agreement with the observational results of Carlson (1969) and the results presented here. The results give evidence of easterly wave growth across the q_y sign reversal region in the 10-yr climatology.

b. Australia

The results for Africa largely confirm previous findings, except that the role of deep convection in creating a positive PV anomaly and contributing to the sign reversal has been quantified using observed OLR. The similar alignment of the geography in Australia and West Africa suggests that comparable mechanisms may be at work. In this section the similarities and differences between Africa and Australia will be examined. In the Southern Hemisphere, of course, PV will generally be negative. Because the background (earth) vorticity still increases northward, the Charney–Stern necessary condition in the Southern Hemisphere is still satisfied by a northward decrease of PV.

The December–March 10-yr mean PV, and the region where $\overline{q_y}$ is less than zero, are shown on the 315-K surface in Fig. 8. The 315-K surface is near 700 hPa over most of Australia and the surrounding waters. Between the equator and 10°S the magnitude of the time-mean PV decreases markedly (Fig. 10). Poleward of 10°S the magnitude of the PV slowly decreases, reaching a minimum over northwestern Australia. Although the sign reversal exists on the 310- and 320-K surfaces, the difference in PV between the local PV maximum and minimum is greatest on the 315-K surface. The sign reversal is located along the northern coast of Australia, extending from the Gulf of Carpentaria westward to the eastern Indian Ocean. Thus the Charney–Stern necessary condition for instability is satisfied in the Australian mean fields. The Australian sign reversal is approximately 2000 km shorter in the zonal direction than the African sign reversal.

A plot of the mean isotachs for Australia (Fig. 9) shows an easterly jet collocated with the sign reversal. The Australian jet satisfies the additional Fjortoft condition for instability of the mean flow. The maximum speed of the Australian jet is approximately half that of the African easterly jet (Fig. 2), consistent with the smaller mean meridional temperature gradient (not shown). The PV anomalies were calculated using $\overline{q} - gf/[\overline{\sigma}]$ and are shown in Fig. 10. The stability is averaged over the plotting domain shown in Fig. 8. Cyclonic PV anomalies are found north of Australia extending from the eastern Indian Ocean to the western South Pacific. The strongest cyclonic anomaly is located from 120° to 150°E. A large anticyclonic anomaly is found over the Great Sandy Desert in western Australia. As in Africa, the anticyclonic anomaly is very likely driven by an upward decrease of diabatic heating over the Australian desert. The presence of a deep mixed layer over the desert maintains the anticyclonic PV anomaly in the lower troposphere. This anomaly to the south plus the cyclonic PV anomaly to the north are associated with a sign change of $\overline{q_y}$ (Fig. 10). The magnitude of the PV anomalies is similar to those in West Africa (Fig. 3).

The convective heating [Eq. (3)] and its relation to $\overline{q_y}$ in the Australian region is shown in Fig. 11. The maximum deep convection is located near the equator across Indonesia and New Guinea. As in Africa, the Australian sign reversal of the meridional PV gradient occurs where the mean meridional gradient of convective heating is largest. This is found near the northern Australian coast between the deep cumulus convection on the equatorward side and dry convection on the poleward side. Although the deepest convection is located well away from the sign reversal in Australia, the meridional gradient of heating across the sign reversal is similar to that observed in Africa (Fig. 4).

The total convective forcing of PV on an isentropic

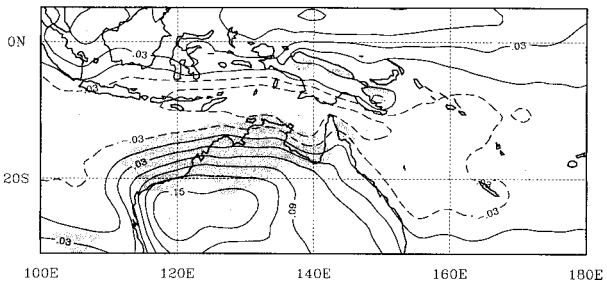

FIG. 10. As in Fig. 8 but for PV anomalies, given by $\overline{q} - gf/[\overline{\sigma}]$ (contoured). Contour interval is 0.03 PVU.

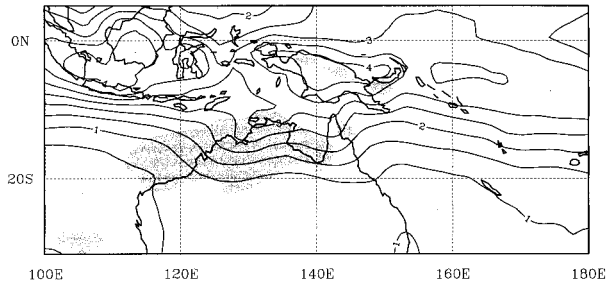

FIG. 11. As in Fig. 8 but for vertically integrated diabatic heating from Eq. (3) (contoured). Contour interval is 0.5°C day^{-1}.

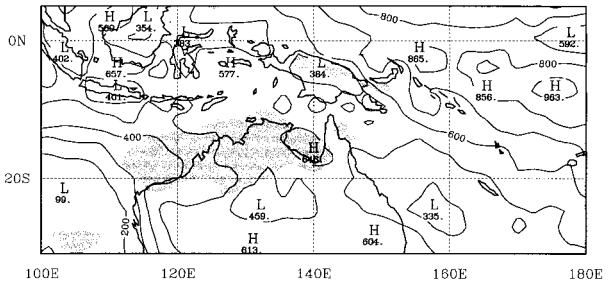

FIG. 13. As in Fig. 8 but for 2–10-day OLR variance (contoured). Contour interval is 100 W^2 m^{-4}.

surface [sum of the first two rhs terms of Eq. (2)] is shown in Fig. 12 (negative values denote cyclonic PV forcing in the Southern Hemisphere). Similar to Africa, the first rhs term of Eq. (2) acts to partially offset the second term and focuses the total convective forcing of PV (Fig. 12) on the equatorward side of the sign reversal. The large convective forcing and associated PV gradient sign reversal on the equatorward side of New Guinea may be a result of the strong convective heating maximum over the island (Fig. 11). There is excellent agreement between the location of the cyclonic PV anomaly (Fig. 10) and calculated total convective forcing of PV (Fig. 12).

Time-mean streamlines (Fig. 9) show that the flow is easterly or southeasterly across northern Australia. Parcels traveling in this flow would pass through the generation region and continually gain cyclonic PV (Fig. 10). As in Africa, the estimated PV change following a parcel can be obtained by using the mean wind, the strength of the total convective forcing of PV, and length of the forcing region. The mean flow in Fig. 9 suggests that, on average, a parcel will move at 4 m s^{-1} and travel about 1700 km before leaving the region of large convective forcing (Fig. 12). Over the 5 days of its passage, assuming an average PV source of 30×10^{-3} PVU day^{-1} (Fig. 12), PV would change on the order of 0.1 PVU, which is consistent with the PV anomaly field shown in Fig. 10. The consistency between the PV gradient from the ECMWF analyses, OLR-derived heating, and total convective forcing of PV give confidence in the ECMWF analyses in the vicinity of Australia.

The results have shown that, like in Africa, the necessary conditions for instability of the mean flow (Charney–Stern and Fjortoft conditions) are satisfied along the northern Australian coast. Thus disturbances in the easterlies may be able to grow by extracting energy from the jet. Since the preferred timescale of disturbances is unknown in the Southern Hemisphere, mean $\widetilde{\mathrm{OLR}}_{2-6}$, $\tilde{V}_{2-6}$, $\widetilde{\mathrm{OLR}}_{2-10}$, and $\tilde{V}_{2-10}$ variances were examined. For brevity only the $\widetilde{\mathrm{OLR}}_{2-10}$ and $\tilde{V}_{2-10}$ variances will be shown here. While the spatial distribution of the 2–6 and 2–10-day variances was very similar, the amplitude of the 2–10-day variance was approximately 50% larger.

Unlike in Africa, no discernible axis of maximum $\widetilde{\mathrm{OLR}}_{2-10}$ variance is found along the Australian sign reversal (Fig. 13). In the Australian region, the $\widetilde{\mathrm{OLR}}_{2-10}$ variance accounts for less than 25% of the total unfiltered OLR variance. The largest variances are found in the western end of the South Pacific convergence zone described by Kiladis et al. (1989). A broad $\widetilde{\mathrm{OLR}}_{2-10}$ variance maximum is present north of Australia with a local maximum located in the Gulf of Carpentaria. Variance values decrease westward from the Gulf of Carpentaria. Low variance values are present along the eastern Australian coast. The regions of large power in the 3–10-day band shown in the 1-yr study by Nakazawa (1986) are not present in the 10-yr mean (Fig. 13).

The $\tilde{V}_{2-10}$ variance for the Australian region is shown in Fig. 14. The $\tilde{V}_{2-10}$ variance accounts for roughly 25%–35% of the total unfiltered v variance across northern Australia. Large 2–10-day variance is found poleward of 25°S due to synoptic-scale disturbances in the mid-

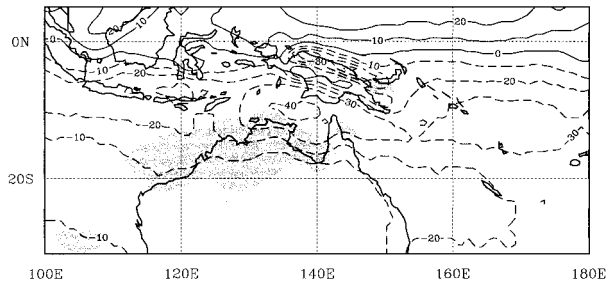

FIG. 12. As in Fig. 8 but for the total convective forcing of PV (contoured). Contour interval is 10×10^{-3} PVU day^{-1}.

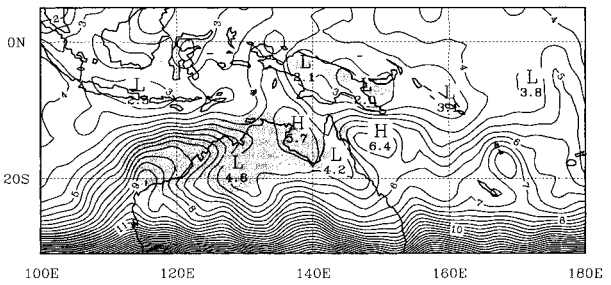

FIG. 14. As in Fig. 8 but for 2–10-day v variance (contoured). Contour interval is 0.5 m^2 s^{-2}.

latitude westerlies. Three distinct variance maxima are found: the first is located just to the east of the Australian coast upstream of the sign reversal, the second is located in the Gulf of Carpentaria, and the third is found along the sign reversal region in western Australia. All three of these locations are favored regions for tropical cyclogenesis (McBride 1995). The region of large $\tilde{V}_{2-10}$ variance along the northwestern coast appears to extend equatorward from the higher latitudes. The variance maxima over the Gulf of Carpentaria and the east coast of Australia are localized. Neither maximum appears to be the result of growth along the sign reversal. The results from the OLR_{2-10} and $\tilde{V}_{2-10}$ variance calculations do not support the existence of growing disturbances along the Australian sign reversal.

4. Discussion

Burpee (1972) documented the existence of a sign reversal of the meridional PV gradient over Africa. This sign reversal satisfies the necessary condition for instability of the mean flow (Charney and Stern 1962). Burpee suggested that this instability was the source of African easterly waves. The latitudinal distribution of ocean and desert in Australia is similar to that in West Africa. This suggests that Charney–Stern criterion may be satisfied there as well. Ten years of ECMWF analyses and OLR data are used to construct a long-term climatology of the African and Australian sign reversal and measures of easterly wave disturbances.

In both Africa and Australia, sign reversals of the meridional PV gradient are located where the meridional gradient of convective heating is largest on the poleward side of the maximum deep convection. A PV budget analysis [Eq. (2)], using OLR as a proxy for convective heating, is performed. In this calculation the vertical advection of PV is treated as a source term. The results show that the total convective forcing of PV (sum of the vertical advection and convective generation terms) is largest on the equatorward edge of the sign reversal. The effect of dry convection as a PV sink on the poleward side of the sign reversal region is not accounted for by Eq. (3). In both the African and Australian regions the anticyclonic PV anomaly driven by dry convection over the desert was larger in area and magnitude than the cyclonic PV anomaly due to deep cumulus convection. The anticyclonic PV anomaly also plays a major role in creating the sign reversal.

Variances of the meridional component of the horizontal wind and OLR are used to evaluate the possible existence of growing disturbances. Large $\widetilde{\mathrm{OLR}}_{2-6}$ variance is found within and downstream of the African sign reversal region. The location of the $\widetilde{\mathrm{OLR}}_{2-6}$ variance is in agreement with the previous work of Nitta et al. (1985) and Nakazawa (1986), as well as the convective storm climatologies of Thorncroft and Haile (1995), Hodges and Thorncroft (1997), and Laing and Fritsch (1997). However, the $\widetilde{\mathrm{OLR}}_{2-6}$ variance does not appreciably increase westward, indicating that it is not a good measure of strengthening easterly waves. The $\tilde{V}_{2-6}$ variance shows a substantial westward increase along the sign reversal. The growth of $\tilde{V}_{2-6}$ variance implies an increase in disturbance amplitude. Decay of the variance is observed west of the African coast in the Atlantic.

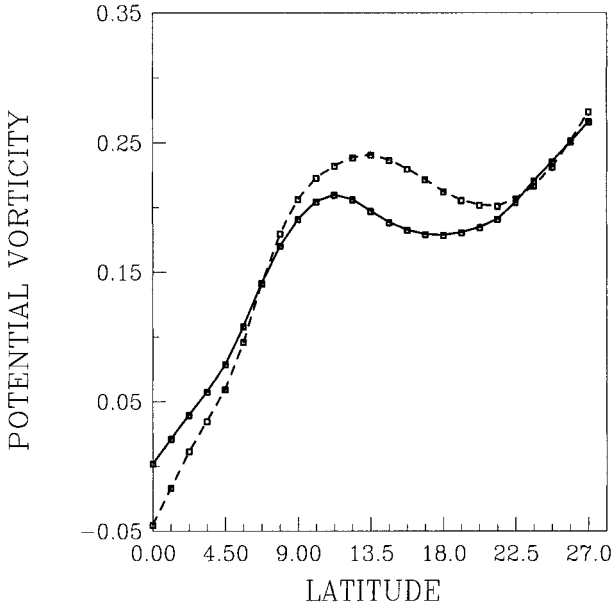

FIG. 15. The 10-yr summertime mean PV (in PVU) distribution with latitude, averaged along the sign reversal, for the African (solid) and Australian (dashed) regions. PV in Australia is multiplied by −1.

In Australia $\tilde{V}_{2-10}$ variance maxima were found in locations where tropical cyclones are favored (McBride 1995). No sign of disturbance growth was observed in the $\tilde{V}_{2-10}$ and $\widetilde{\mathrm{OLR}}_{2-10}$ variance calculations along the Australian sign reversal. One possible explanation for the lack of growth would be that the Australian sign reversal is weaker than the African sign reversal and is unable to produce and maintain growing disturbances. Figure 15 shows the distribution of PV with respect to latitude averaged along the sign reversal for the African (solid) and Australian (dashed) regions. The distribution of PV is similar between the two regions, and the difference in PV between the ITCZ/monsoon trough maximum and the poleward minimum is nearly the same for the two regions. Given this similarity between the African and Australian sign reversals, it is unclear why evidence of growing disturbances (as measured by bandpass-filtered variances) was not found in the Australian region. One factor that may play a role in the lack of wave growth in Australia is the length scale of the unstable region. The Australian region is about 3000 km in length, nearly equal to the typical wavelength of easterly waves in other latitudes. The unstable region in Africa is about 5000 km in length. The relatively short Australian sign reversal may not allow sufficient time for waves to grow, or may be insufficient to produce

reinvigoration of preexisting waves of 2500–3000-km wavelength.

Terrain has also been suggested as a forcing mechanism for AEWs. The east African highlands (Carlson 1969; Frank 1970) and the Hoggar Mountains (Reed et al. 1988; Mozer and Zehnder 1996) are located near the climatological sign reversal region. Easterly flow impinging on these mountains may produce the initial disturbances that subsequently grow on the unstable basic state. The lack of such large terrain features within or upstream of the sign reversal may represent an additional factor in the apparent scarcity of such disturbances in Australia. Alternatively, given that the Charney–Stern condition is necessary but not sufficient, it may be that the flow is simply not unstable.

It is apparent from this and previous work (Brikas and Thorncroft 1999; Thorncroft and Blackburn 1999) that both deep and shallow convective heating play a major role in the generation of the PV gradient sign reversals over Africa and Australia. The role of the mean meridional circulation and of the waves themselves remains uncertain. A full PV budget will be required to address these factors.

Acknowledgments. This research was supported by Office of Naval Research Grant N000149810599 and the National Science Foundation through Grant ATM9900671. The authors would like to thank Dr. Lloyd Shapiro, Dr. Michael Reeder, David Vollaro, and two anonymous reviewers for their useful comments. The first author would like to thank Cathy Smith of the University of Colorado for her assistance in obtaining the OLR data. The GOES Precipitation Index dataset is available via anonymous ftp at ftp://daac.gsfc.nasa.gov/data/hydrology/precip/arkin/gpcp_gpi/. The CPC Merged Analysis of Precipitation is available via anonymous ftp at ftp.cdc.noaa.gov. The Global Precipitation Climatology Project version 1c satellite–gauge precipitation product (Huffman et al. 1995) is available via anonymous ftp at ftp://daac.gsfc.nasa.gov/data/hydrology/precip/gpcp.

REFERENCES

Albignat, J. P., and R. J. Reed, 1980: The origin of African wave disturbances during Phase III of GATE. *Mon. Wea. Rev.,* **108,** 1827–1839.

Arkin, P. A., and B. N. Meisner, 1987: The relationship between large-scale convective rainfall and cold cloud over the western hemisphere during 1982–84. *Mon. Wea. Rev.*, **115,** 51–74.

Avila, L. A., and G. B. Clark, 1989: Atlantic tropical systems of 1988. *Mon. Wea. Rev.,* **117,** 2260–2265.

——, and R. J. Pasch, 1992: Atlantic tropical systems of 1991. *Mon. Wea. Rev.,* **120,** 2688–2696.

Brikas, D., and C. D. Thorncroft, 1999: Maintenance of the African easterly jet. Preprints, *23d Conf. on Hurricanes and Tropical Meteorology,* Dallas, TX, Amer. Meteor. Soc., 897–900.

Burpee, R. W., 1972: The origin and structure of easterly waves in the lower troposphere of North America. *J. Atmos. Sci.,* **29,** 77–90.

——, 1974: Characteristics of North African easterly waves during the summers of 1968 and 1969. *J. Atmos. Sci.,* **31,** 1556–1570.

Carlson, T. N., 1969: Some remarks on African wave disturbances and their progress over the tropical Atlantic. *Mon. Wea. Rev.,* **97,** 716–726.

Chang, C.-P., J. M. Chen, P. A. Harr, and L. E. Carr, 1996: Northwestward-propagating wave patterns over the tropical western North Pacific during summer. *Mon. Wea. Rev.,* **124,** 2245–2266.

Charney, J. G., and M. E. Stern, 1962: On the stability of internal baroclinic jets in a rotating atmosphere. *J. Atmos. Sci.,* **19,** 159–172.

Cook, K. H., 1999: Generation of the African easterly jet and its role in determining West African precipitation. *J. Climate,* **12,** 1165–1184.

Duchon, C. E., 1979: Lanczos filtering in one and two dimensions. *J. Appl. Meteor.,* **18,** 1016–1022.

Dunkerton, T. J., and M. P. Baldwin, 1995: Observation of 3–6-day meridional wind oscillations over the tropical Pacific, 1973–1992: Horizontal structure and propagation. *J. Atmos. Sci.,* **52,** 1585–1601.

Eliassen, A., 1983: The Charney–Stern theorem on barotropic-baroclinic instability. *Pure Appl. Geophys.,* **121,** 563–573.

Fjortoft, R., 1950: Application of integral theorems in deriving criteria of stability for laminar flows and for the baroclinic circular vortex. *Geofys. Publ.,* **17,** 1–52.

Frank, N. L., 1970: Atlantic tropical systems of 1969. *Mon. Wea. Rev.,* **98,** 307–314.

Harrison, D. E., and G. A. Vecchi, 1997: Westerly wind bursts in the tropical Pacific, 1986–95. *J. Climate,* **10,** 3131–3155.

Hodges, K. I., and C. D. Thorncroft, 1997: Distribution and statistics of African mesoscale convective weather systems based on ISCCP Meteostat imagery. *Mon. Wea. Rev.,* **125,** 2821–2837.

Hoskins, B. J., M. E. McIntyre, and A. W. Robertson, 1985: On the use and significance of isentropic potential vorticity maps. *Quart. J. Roy. Meteor. Soc.,* **111,** 877–946.

Houze, R. A., 1997: Stratiform precipitation in regions of convection: A meteorological paradox? *Bull. Amer. Meteor. Soc.,* **78,** 2179–2196.

Huffman, G. J., R. F. Adler, B. Rudolf, U. Schneider, and P. R. Keehn, 1995: Global precipitation estimates based on a technique for combining satellite-based estimates, rain gauge analysis, and NWP model precipitation information. *J. Climate,* **8,** 1284–1295.

Janowiak, J. E., and P. E. Arkin, 1991: Rainfall variations in the tropics during 1986–1989. *J. Geophys. Res.,* **96,** 3359–3373.

Kiladis, G. N., H. von Storch, and H. van Loon, 1989: Origin of the South Pacific convergence zone. *J. Climate,* **2,** 1161–1171.

Laing, A. G., and J. M. Fritsch, 1997: The global population of mesoscale convective complexes. *Quart. J. Roy. Meteor. Soc.,* **123,** 389–405.

Lanczos, C., 1956: *Applied Analysis.* Prentice-Hall, 539 pp.

Lau, K.-H., and N.-C. Lau, 1990: Observed structure and propagation characteristics of tropical summertime disturbances. *Mon. Wea. Rev.,* **118,** 1888–1913.

Liebmann, B., and H. Hendon, 1990: Synoptic-scale disturbances near the equator. *J. Atmos. Sci.,* **47,** 1463–1479.

——, and C. Smith, 1996: Description of a complete (interpolated) outgoing longwave radiation dataset. *Bull. Amer. Meteor. Soc.,* **77,** 1275–1276.

McBride, J. L., 1995: Tropical cyclone formation. *Global Perspectives on Tropical Cyclones,* R. Elsberry, Ed., World Meteorological Organization Rep. TCP-38, 63–105.

——, and T. D. Keenan, 1982: Climatology of tropical cyclone genesis in the Australian region. *J. Climatol.,* **2,** 13–33.

Molinari, J., S. Skubis, and D. Vollaro, 1995: External influences on hurricane intensity. Part III: Potential vorticity evolution. *J. Atmos. Sci.,* **52,** 3593–3606.

——, D. Knight, M. Dickinson, D. Vollaro, and S. Skubis, 1997: Potential vorticity, easterly waves, and tropical cyclogenesis. *Mon. Wea. Rev.,* **125,** 2699–2708.

——, D. Vollaro, S. Skubis, and M. Dickinson, 2000: Origins and

mechanisms of eastern Pacific tropical cyclogenesis: A case study. *Mon. Wea. Rev.*, **128,** 125–139.
Mozer, J. B., and J. A. Zehnder, 1996: Lee vorticity production by large-scale tropical mountain ranges. Part II: A mechanism for the production of African waves. *J. Atmos. Sci.*, **53,** 539–549.
Nakazawa, T., 1986: Intraseasonal variations of OLR in the tropics during the FGGE year. *J. Meteor. Soc. Japan,* **64,** 17–33.
Nitta, T., Y. Nakagomi, Y. Suzuki, N. Hasegawa, and A. Kadokura, 1985: Global analysis of the lower tropospheric disturbances in the tropics during northern summer of the FGGE year. Part I: Global feature of disturbances. *J. Meteor. Soc. Japan,* **63,** 1–19.
Norquist, D. C., E. E. Recker, and R. J. Reed, 1977: The energetics of African wave disturbances as observed during phase III of GATE. *Mon. Wea. Rev.*, **105,** 334–342.
Pytharoulis, I., and C. Thorncroft, 1999: The low-level structure of African easterly waves in 1995. *Mon. Wea. Rev.*, **127,** 2266–2280.
Raymond, D. J., 1992: Nonlinear balance and potential vorticity thinking at large Rossby number. *Quart. J. Roy. Meteor. Soc.*, **118,** 987–1015.
Reed, R. J., D. C. Norquist, and E. E. Recker, 1977: The structure and properties of African wave disturbances as observed during phase III of GATE. *Mon. Wea. Rev.*, **105,** 317–333.
——, A. Hollingsworth, W. A. Heckley, and F. Delsol, 1988: An evaluation of the performance of the ECMWF operational system in analyzing and forecasting easterly wave disturbances over Africa and the tropical Atlantic. *Mon. Wea. Rev.*, **116,** 824–865.
Riehl, H., 1954: *Tropical Meteorology.* McGraw-Hill, 392 pp.
Rodwell, M. J., and B. J. Hoskins, 1995: A model of the Asian summer monsoon. Part II: Cross-equatorial flow and PV behavior. *J. Atmos. Sci.*, **52,** 1341–1356.
Sardeshmukh, P. D., and B. Liebmann, 1993: An assessment of low-frequency variability in the tropics as indicated by some proxies of tropical convection. *J. Climate,* **6,** 569–575.
Schubert, W. H., P. E. Ciesielski, D. E. Stevens, and H.-C. Kuo, 1991: Potential vorticity modeling of the ITCZ and the Hadley circulation. *J. Atmos. Sci.*, **48,** 1493–1509.
Simpson, R. H., N. L. Frank, D. Shideler, and H. M. Johnson, 1969: Atlantic tropical disturbances of 1968. *Mon. Wea. Rev.*, **97,** 240–255.
Thorncroft, C. D., and B. J. Hoskins, 1994a: An idealized study of African easterly waves. Part I: A linear view. *Quart. J. Roy. Meteor. Soc.*, **120,** 953–982.
——, and ——, 1994b: An idealized study of African easterly waves. Part II: A nonlinear view. *Quart. J. Roy. Meteor. Soc.*, **120,** 983–1016.
——, and M. Haile, 1995: The mean dynamic and thermodynamic fields for July 1989 over tropical North Africa and their relationship to convective storm activity. *Mon. Wea. Rev.*, **123,** 3016–3031.
——, and M. Blackburn, 1999: Maintenance of the African easterly jet. *Quart. J. Roy. Meteor. Soc.*, **125,** 763–786.
Tomas, R. A., and P. J. Webster, 1997: The role of inertial instability in determining the location and strength of near-equatorial convection. *Quart. J. Roy. Meteor. Soc.*, **123,** 1445–1482.
——, J. R. Holton, and P. J. Webster, 1999: The influence of cross-equatorial pressure gradients on the location of near-equatorial convection. *Quart. J. Roy. Meteor. Soc.*, **125,** 1107–1127.
Xie, P., and P. A. Arkin, 1997: A 17-year monthly analysis based on gauge observations, satellite estimates, and numerical model outputs. *Bull. Amer. Meteor. Soc.*, **78,** 2539–2558.